Supporting Information for "Geodynamic Modeling with Uncertain Initial Geometries"

A. Spang [1], T. S. Baumann [1], B. J. P. Kaus [1,2]

[1]Johannes Gutenberg University, Institute of Geosciences, Johann-Joachim-Becher-Weg 21, 55128 Mainz, Germany

[2]TeMaS, Terrestrial Magmatic Systems Research Center, temas.uni-mainz.de

Contents of this file

1. Texts S1 to S3
2. Figure S1 to S8
3. Table S1 to S3

Corresponding author: A. Spang, Department of Geosciences, Johannes Gutenberg University, Johann-Joachim-Becher-Weg 21, 55128 Mainz, Germany. (arspang@uni-mainz.de)

December 10, 2021, 12:18pm

Introduction

This file contains supplementary texts about methodology (S1: Additional Options, S2: Model Details) and a simple inversion example for the subduction application (S3: Inverting for Initial Angle). Furthermore, it contains the supplementary Figures S1 to S3 associated with methodology, Figures S4 to S6 associated with Application I: Salt, Figure S7 associated with Application II: Subduction and Figure S8 associated with text S3. Finally, supplementary tables S1 and S2 containing the material parameters used and table S3 containing scaling parameters used in Application I: Salt.

Text S1: Additional Options

Text S1.1: Absolute Transformation Parameters

One issue of the method described in section 2.1.3 is that the absolute change in coordinates of polygon nodes is determined by the size of the polygon. In Figure S1b, the central polygon (lowermost control polygon) is elongated by 0.5 units in y-direction while the lowermost polygon is only elongated by 0.015 units. If this effect is not desired, we offer a second transformation algorithm which works with absolute transformation parameters (dx and dy). dx and dy are the maximum transformations per direction and they are scaled for every node on the polygon, depending on the node's position:

$$\left(\vec{x}_{new} \;\; \vec{y}_{new}\right) = \left(\vec{x} \;\; \vec{y}\right) + \left(\frac{\vec{x}'}{|\overrightarrow{xy}|} \;\; \frac{\vec{y}'}{|\overrightarrow{xy}|}\right) * \begin{pmatrix} dx & 0 \\ 0 & dy \end{pmatrix} \tag{S1}$$

$$|\overrightarrow{xy}|_n = \sqrt{{x'_n}^2 + {y'_n}^2} \tag{S2}$$

The fraction in equation S1 corresponds to element-wise division. The lower half of the body in Figure S1c was changed with absolute transformation parameters. While the central polygon (lowermost control polygon) is identical to the one in Figure S1b, all polygons below are wider, most notably the lowest one. Figure S2a shows how the different methods affect the lowermost polygon. The approach of absolute transformation is limited when it comes to shrinking parts of the body which have very small polygons.

Text S1.2: Coordinate rotation

The body might have a preferred orientation which is not aligned with either the x- or the y-direction, so scaling it in a different direction might be desirable. To do that, we include the option to rotate the coordinate system such that the orientation, in which transformation is preferred, aligns with one of the axes. This is done by defining the rotation matrix

$$Q = \begin{pmatrix} cos(\theta) & sin(\theta) \\ -sin(\theta) & cos(\theta) \end{pmatrix} \tag{S3}$$

where θ represents the preferred direction of transformation and rotates the coordinate system clockwise. To apply it, equation 3 has to be modified to:

$$\begin{pmatrix} \vec{x}_{i,new} & \vec{y}_{i,new} \end{pmatrix} = \begin{pmatrix} \vec{x_i}' & \vec{y_i}' \end{pmatrix} * Q * \begin{pmatrix} Sx_1 & 0 \\ 0 & Sy_1 \end{pmatrix} * Q^T + \begin{pmatrix} x_{i_c} & y_{i_c} \\ ... & \\ x_{i_c} & y_{i_c} \end{pmatrix} \tag{S4}$$

Figure S2b shows an example case where a polygon is elongated in NNE-SSW direction, so without rotating the coordinate system it would not be possible to only transform the polygon along its longest axis. However, by rotating the y-axis to align with the orientation, then apply the scaling and rotate it back, we can. Figure S2c shows that more complex shapes can be handled in the same way.

Text S2.1: LaMEM

For our models, we utilize the thermomechanical finite differences code LaMEM (Kaus et al., 2016). It solves for the conservation of momentum, mass and energy (eq. S5-S7), using a staggered grid in combination with a marker-in-cell approach (Harlow & Welch, 1965).

$$\frac{\partial \tau_{ij}}{\partial x_j} - \frac{\partial p}{\partial x_i} + \rho g_i = 0 \tag{S5}$$

$$\frac{1}{K}\frac{Dp}{Dt} - \alpha \frac{DT}{Dt} + \frac{\partial v_i}{\partial x_i} = 0 \tag{S6}$$

$$\rho C_p \frac{DT}{Dt} = \frac{\partial}{\partial x_i}\left(\lambda \frac{\partial T}{\partial x_i}\right) \tag{S7}$$

τ_{ij} is the Cauchy stress deviator, $x_i (i = 1, 2, 3)$ denotes the Cartesian coordinates, p is pressure (positive in compression), ρ density, g_i gravitational acceleration, K the bulk modulus, α the thermal expansion coefficient, T the temperature, v_i the velocity vector, C_p the specific heat capacity, λ the thermal conductivity and D/Dt is the material time derivative.

The rocks are characterized by a visco-elasto-plastic rheology where the strain rate is the sum of the elastic, viscous and plastic components:

$$\dot{\epsilon}_{ij} = \dot{\epsilon}^{el}_{ij} + \dot{\epsilon}^{vi}_{ij} + \dot{\epsilon}^{pl}_{ij} \tag{S8}$$

$\dot{\epsilon}_{ij}$ denotes the total deviatoric strain rate tensor, while $\dot{\epsilon}^{el}_{ij}$, $\dot{\epsilon}^{vi}_{ij}$ and $\dot{\epsilon}^{pl}_{ij}$ represent the elastic, viscous and plastic strain rate components. For a detailed discussion of this equation and all of its components, the reader is referred to Kaus et al. (2016). Here we will focus on the material parameters which impact the 3 components.

The elastic component depends on the shear modulus G:

$$\dot{\epsilon}_{ij}^{el} = \frac{1}{2G}\frac{D\tau_{ij}}{Dt}, \tag{S9}$$

where $D\tau_{ij}/Dt$ is the objective derivative of the stress tensor.

The viscous component depends on the viscosity η:

$$\dot{\epsilon}_{ij}^{vi} = \frac{\tau_{ij}}{2\eta} \tag{S10}$$

η is either a constant (see tables S1 and S2) or follows the stress- and temperature-dependent powerlaw relationship of dislocation creep:

$$\eta = \frac{1}{2}(B_n)^{-\frac{1}{n}}(\dot{\epsilon}_{II})^{\frac{1}{n}-1}\exp\left(\frac{E_n + pV_n}{nRT}\right), \tag{S11}$$

where B_n is the creep constant, $\dot{\epsilon}_{II}$ the square root of the second invariant of the strain rate ($\dot{\epsilon}_{II} = (\frac{1}{2}\dot{\epsilon}_{ij}\dot{\epsilon}_{ij})^{1/2}$), E_n the activation energy, p the pressure, V_n the activation volume, n the powerlaw exponent, R the universal gas constant and T the temperature.

The plastic component is governed by the Drucker-Prager failure criterion (Drucker & Prager, 1952):

$$\tau_{II} \leq \sin(\phi)p + \cos(\phi)c_0 \tag{S12}$$

where τ_{II} is the square root of the second invariant of the stress tensor ($\tau_{II} = (\frac{1}{2}\tau_{ij}\tau_{ij})^{1/2}$), ϕ is the friction angle, p the pressure and c_0 the cohesion. As long as τ_{II} does not exceed the failure criterion, the stress is accommodated by visco-elastic deformation.

Text S2.2: Model Details Application I: Salt

We model a homogeneous slice of crust that is 20 km wide and deep and hosts a 3.5 km thick salt bed from which the diapir rises. Along the boundaries of the model, we employ free slip conditions (velocities normal to boundaries equal zero). At the top of the crust, we use a stabilized (Kaus et al., 2010) stress free internal surface and 5 km thick layer of sticky air (Crameri et al., 2012). We use 128 cells in the horizontal and 256 cells in vertical direction. For simplicity, we use linear viscosities η for all materials. Table S1 summarizes the material parameters that we employed. A shear modulus of 15 GPa and a Poisson's ratio of 0.25 correspond to a Young's modulus of 37.5 GPa which is consistent with previous laboratory and modeling studies on salt (Ingraham et al., 2015, June; Zong et al., 2017; Baumann et al., 2018).

Text S2.3: Model Details Application II: Subduction

Our subduction model is 2000 km wide and extends from the surface to 660 km depth. We use 512 cells in the horizontal and 256 cells in the vertical direction, yielding resolutions of about 4 and 2.5 km respectively. The 100 km thick continent is made up of 40 km of crust and 60 km of lithospheric mantle. We assign different linear temperature gradients to the continental crust and lithosphere and use a half-space cooling model for the subducting plate that corresponds to a thermal age of 30 Myr. As the plate has already started subducting at the start of our simulations, we add another 1 Myr of temperature diffusion to account for the heating during that initial stage of subduction (Figure S7a). All materials are described by a temperature- and stress-dependent visco-plastic rheology. Table S2 summarizes all material parameters. We use free slip boundary conditions along all model edges and do not prescribe any boundary velocities.

Text S3: Inverting for Initial Angle

Reconstructions (e.g. Sdrolias & Müller, 2006) show that convergence velocities between plates fluctuate throughout the evolution of subduction zones. These fluctuations are frequently interpreted to be the result of subdcution of ocean plateaus or ridges (e.g. Martinod et al., 2010) but our models show that the convergence rate also fluctuates without any changes in the elevation or density structure of the oceanic plate. Instead the velocity profile seems to be coupled to the initial dip of the subducting slab (β_0), so given a good understanding of the rheology of the system, a velocity reconstruction could also be used to invert for an initial angle using modeling. To demonstrate the feasibility of this approach, we use a synthetic profile that we generated using $\beta_0 = 72.5°$ (dotted line in Figure S8a). We add normally distributed random noise ($\sigma = 0.5\,\mathrm{cm\,yr^{-1}}$) to the profile to get a synthetic observation in 1 Myr intervals (black circles in Figure S8a). We then run a set of models in 5° intervals (blue in Figure S8b), compute the RMS misfit (Φ) and add models in 1° intervals in areas of low misfit (orange in Figure S8b).

Figure S8b shows that we can find the true β_0 with only a few forward models. In a real application, there might be more parameters involved in the inversion process but as there is an obvious dependency of the velocity profile on the initial angle, an inversion with more models should still converge to the correct solution.

References

Baumann, T. S., Kaus, B., & Popov, A. A. (2018). Deformation and stresses related to the gorleben salt structure: insights from 3d numerical models. *Mechanical Behavior of Salt, Saltmech IX*, 15–27.

Crameri, F., Schmeling, H., Golabek, G. J., Duretz, T., Orendt, R., Buiter, S., ... Tackley, P. (2012). A comparison of numerical surface topography calculations in geodynamic modelling: an evaluation of the 'sticky air'method. *Geophysical Journal International*, *189*(1), 38–54.

Drucker, D. C., & Prager, W. (1952). Soil mechanics and plastic analysis or limit design. *Quarterly of applied mathematics*, *10*(2), 157–165.

Harlow, F. H., & Welch, J. E. (1965). Numerical calculation of time-dependent viscous incompressible flow of fluid with free surface. *The physics of fluids*, *8*(12), 2182–2189.

Ingraham, M. D., Broome, S. T., Bauer, S. J., Barrow, P. C., & Flint, G. M. (2015, June). Behavior of salt from the bayou choctaw salt dome. In *49th US Rock Mechanics/Geomechanics Symposium.*

Kaus, B. J. P., Mühlhaus, H., & May, D. A. (2010). A stabilization algorithm for geodynamic numerical simulations with a free surface. *Physics of the Earth and Planetary Interiors*, *181*(1-2), 12–20.

Kaus, B. J. P., Popov, A. A., Baumann, T., Pusok, A., Bauville, A., Fernandez, N., & Collignon, M. (2016). Forward and inverse modelling of lithospheric deformation on geological timescales. In *Proceedings of NIC Symposium.*

Martinod, J., Husson, L., Roperch, P., Guillaume, B., & Espurt, N. (2010). Horizontal subduction zones, convergence velocity and the building of the Andes. *Earth and*

Planetary Science Letters, *299*(3-4), 299–309.

Sdrolias, M., & Müller, R. D. (2006). Controls on back-arc basin formation. *Geochemistry, Geophysics, Geosystems*, *7*(4).

Zong, J., Stewart, R. R., Dyaur, N., & Myers, M. T. (2017). Elastic properties of rock salt: Laboratory measurements and gulf of mexico well-log analysis. *Geophysics*, *82*(5), D303–D317.

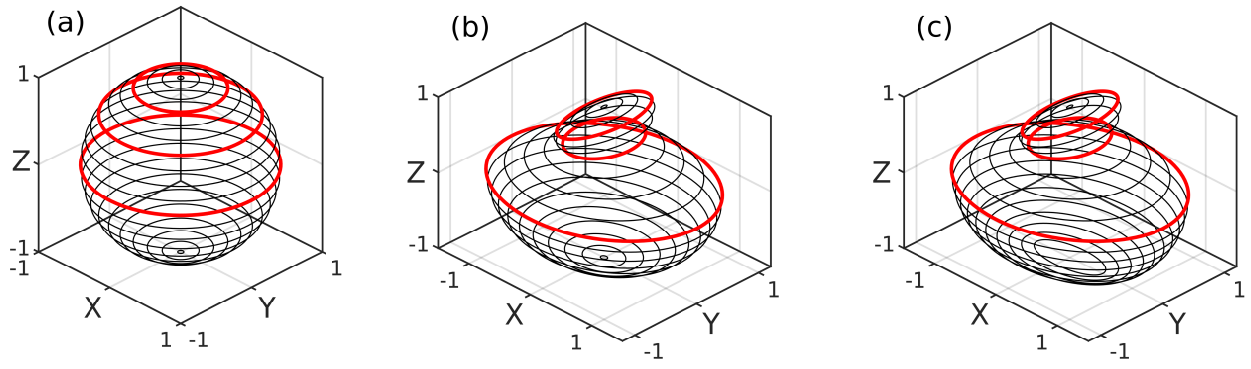

Figure S1. Illustration of 3-dimensional bodies as sets of 2-dimensional polygons. The three red polygons are the control polygons which are used to transform the body. (a) Sphere with radius 1, represented as 21 polygons. (b) Sphere from S1a after transformation by scaling. (c) Sphere from S1a with the upper half being transformed by scaling and the lower half by absolute transformation parameters. Note how the lower half is wider in S1c than in S1b.

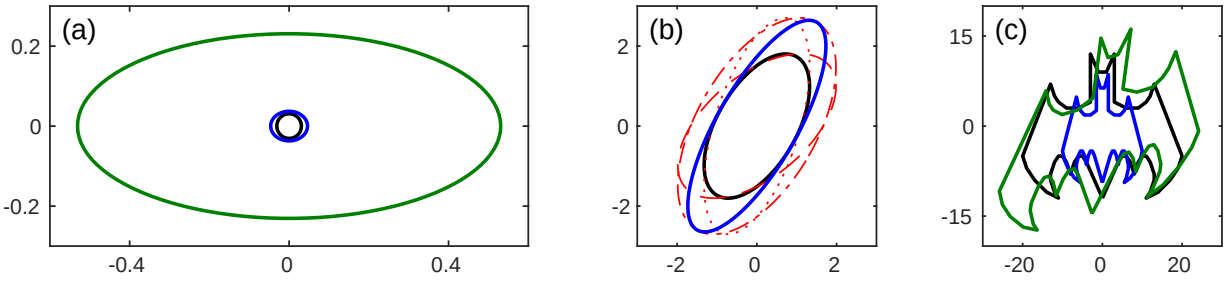

Figure S2. Illustration of how the transformation methods work on single 2-dimensional polygons. (a) Example of how the different transformation methods affect the lowermost polygon in Figure S1. Original in black, scaling in blue (used for Figure S1b) and transformation by absolute values in green (used for Figure S1c). (b) Scaling a polygon with preferred orientation. Original in black, dashed red line: Sx = 1.5, dotted red line: Sy = 1.5, dashed and dotted red line: Sx = Sy = 1.5, blue line: Sy = 1.5 and $\theta = 30$. (c) Illustration of how complex shapes are handled. Original in black, scaled version in blue (Sx = 0.5, Sy = 0.75), scaling and coordinate system rotation in green (Sy = 1.5, $\theta = 45$).

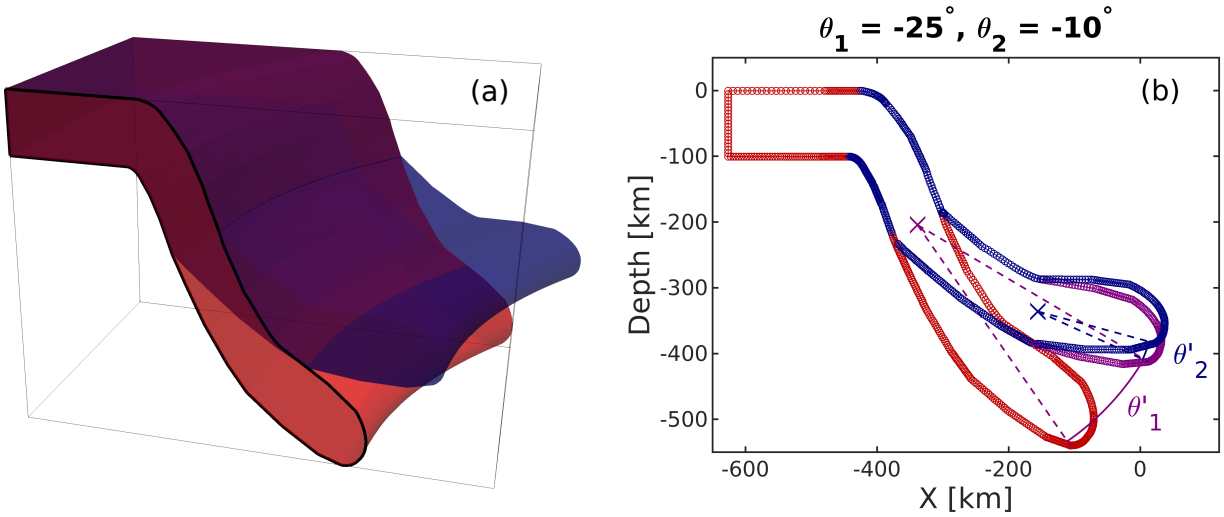

Figure S3. (a) 3D Example of a plate, subducting along a curved trench, drawn in geomIO (red) and an automatically generated variation that is bent at two locations in 200 and 320 km depth (crosses in S3b). Black line shows one of the vertical polygons that the 3D volume is represented as inside our algorithm and is identical to the red polygon in S3b. (b) Representation of the plates in S3a as vertical polygons. Red: original, purple: after the first rotation, blue: after both rotations. Crosses show the centers of rotation.

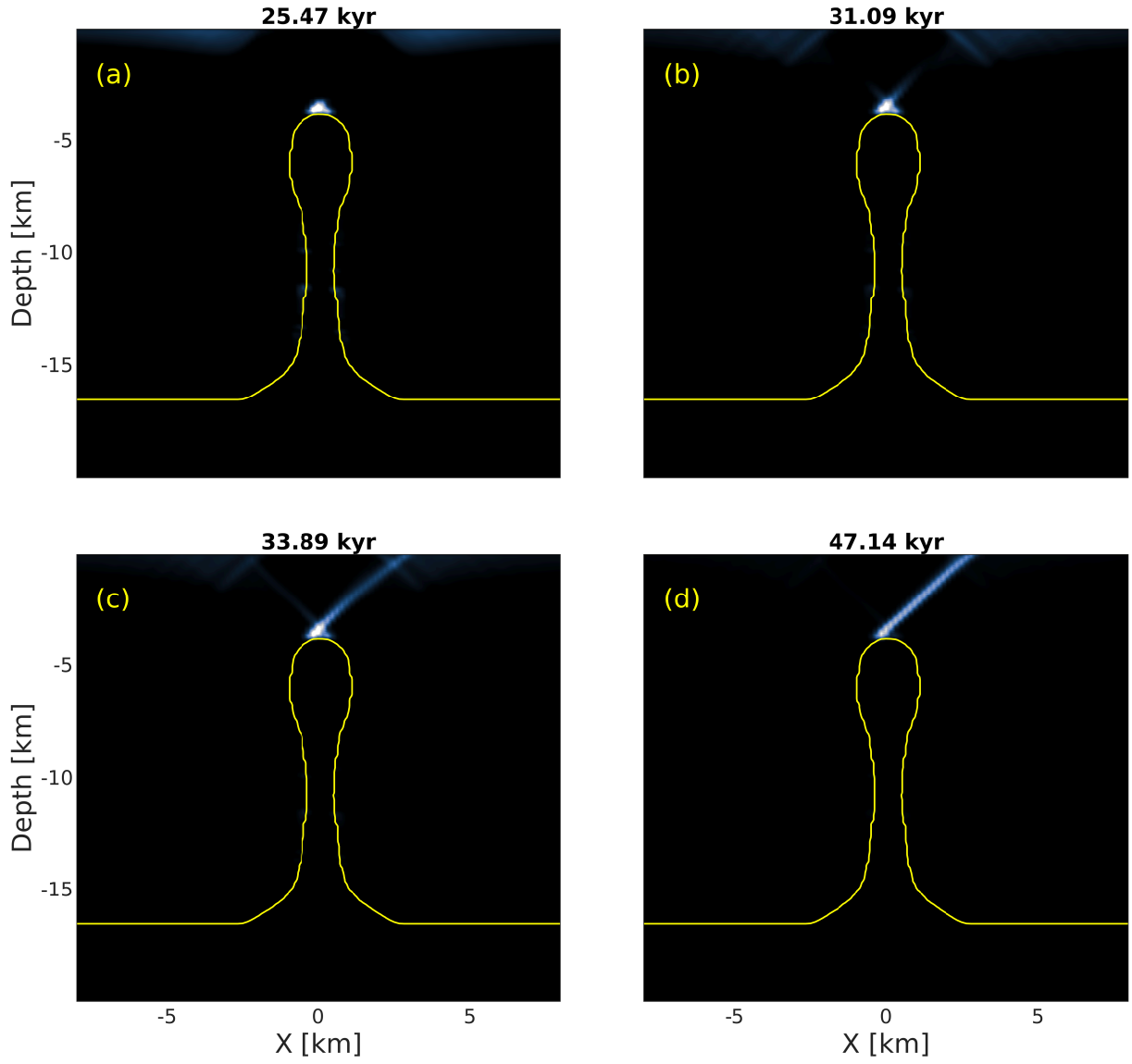

Figure S4. Evolution of plastic strain (i.e. faults) around the synthetic 'true' diapir (blue in Figure 3). (a) Early stage plastic failure along the surface and at the tip of the diapir. (b) First faults start to connect diapir and surface. (c) Faults have connected diapir and surface. Right fault takes up most of the deformation. (d) Right fault takes up all the deformation and left fault is no longer active.

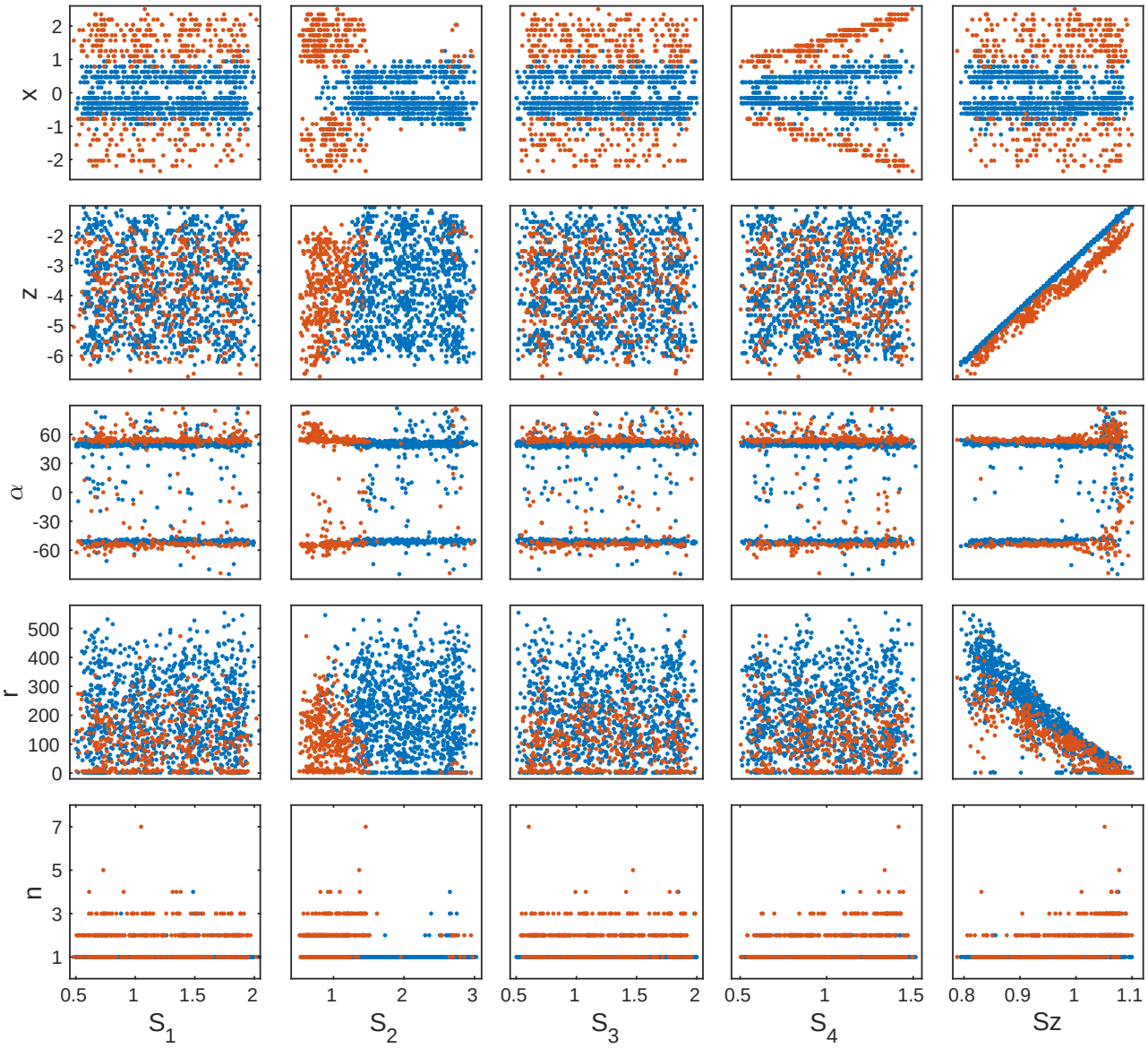

Figure S5. All fault properties in relation to each scaling parameter. x: lateral coordinate of lower fault tip, z: vertical coordinate of lower fault tip, α: dip angle of fault, r: aspect ratio of fault, n: number of faults. Blue dots denote faults that connect to the center and orange dots denote faults that connect to the side of the diapir head. Note that the orange dots are plotted on top which is why they hide a lot of blue dots in the lowest row of sub-figures.

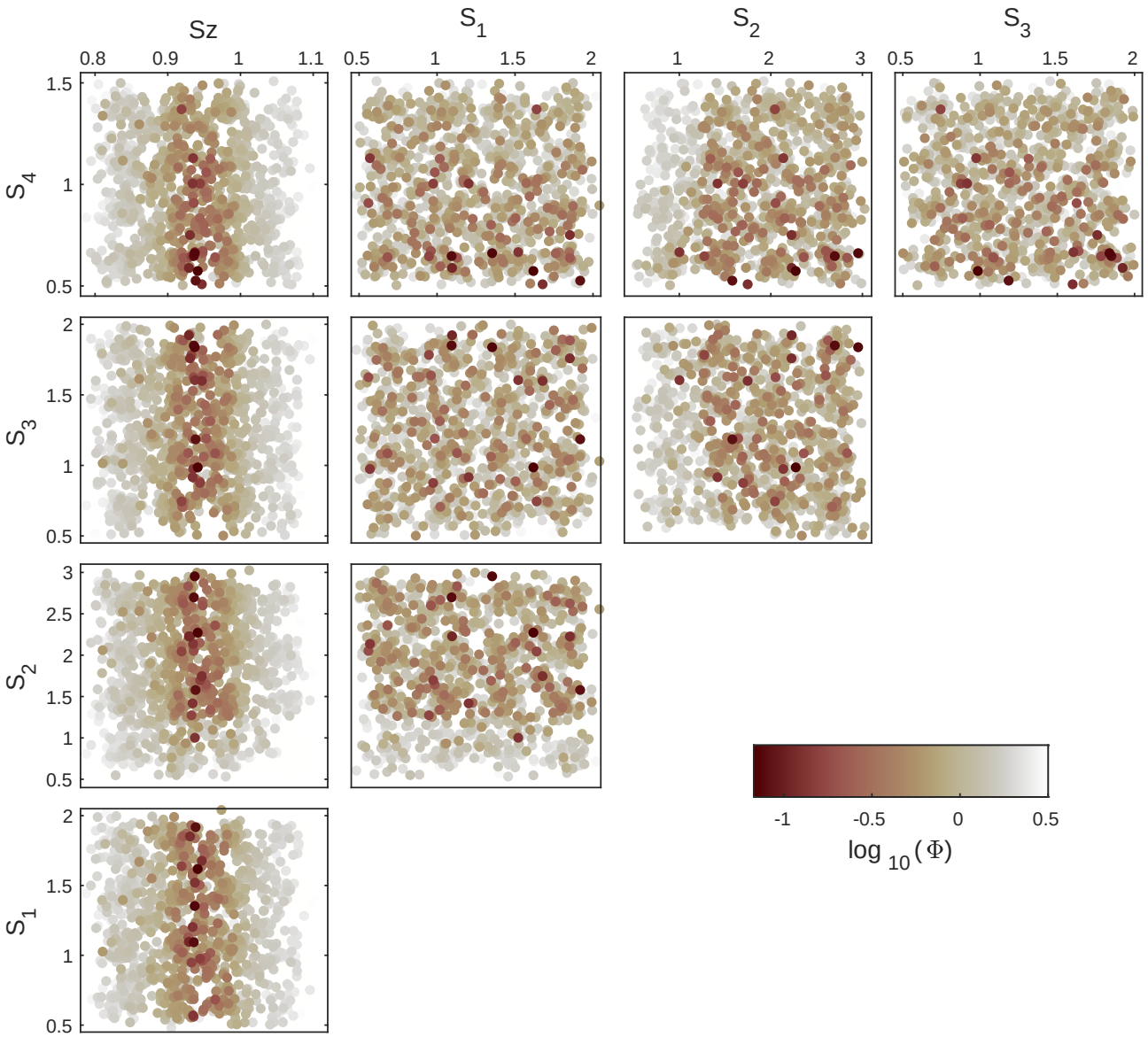

Figure S6. Misfit of the fault systems in dependence of all sets of 2 scaling parameters. Low misfit always correlates with medium Sz values and often correlates with low S_4. High misfit always correlates with low S_2. S_1 and S_3 do not show correlation with the misfit.

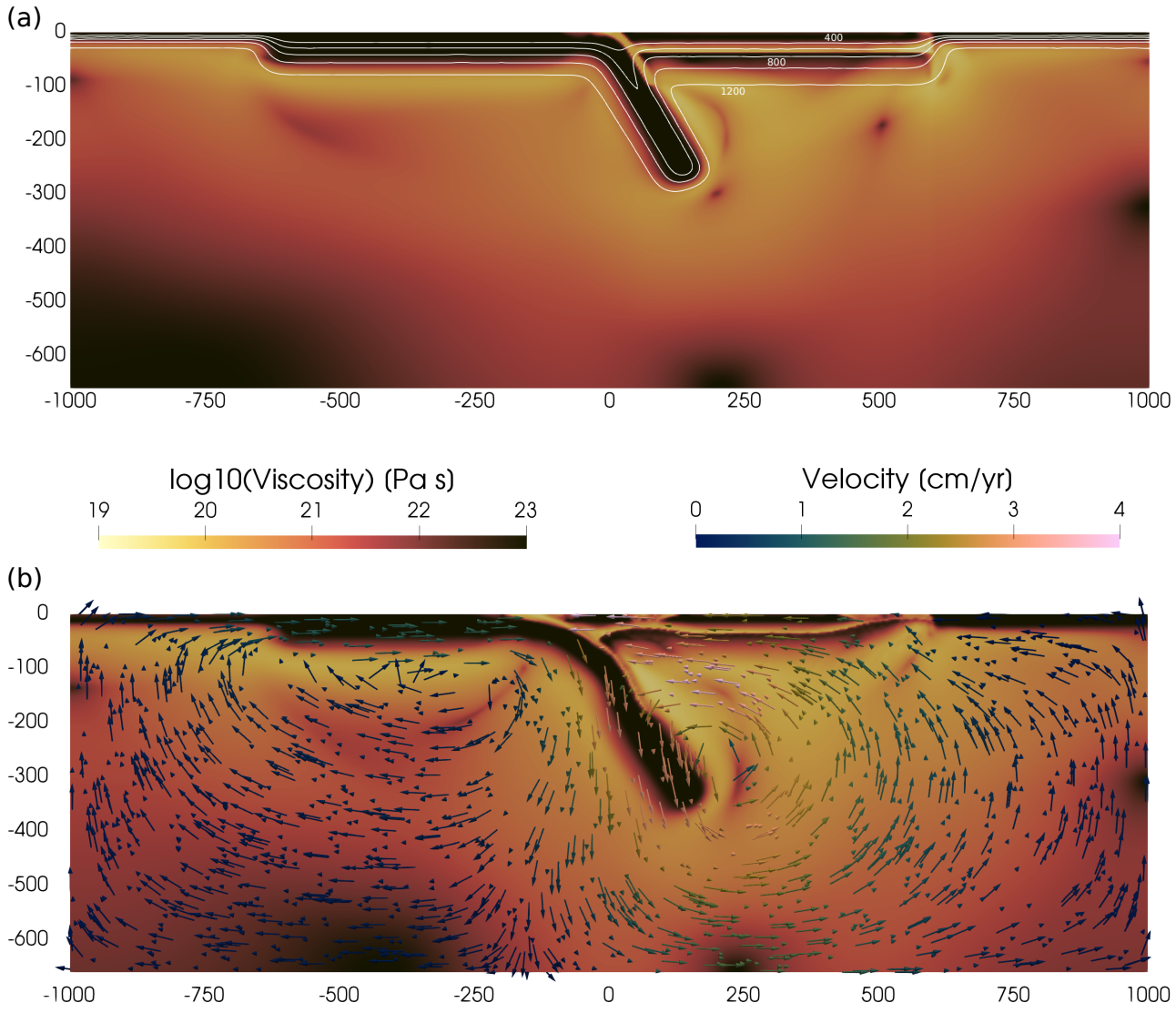

Figure S7. (a) Viscosity in the reference model ($\beta_0 = 60°$) at the first time step. White contour lines show temperature in 200 °C intervals. Top and bottom of the model have temperatures of 0 and 1350 °C respectively. Axes are in km. (b) Snapshot of the same model after 2 Myr. Slab has started to sink, trench has started retreating and continent has undergone buckling and extension. Arrows show velocity field.

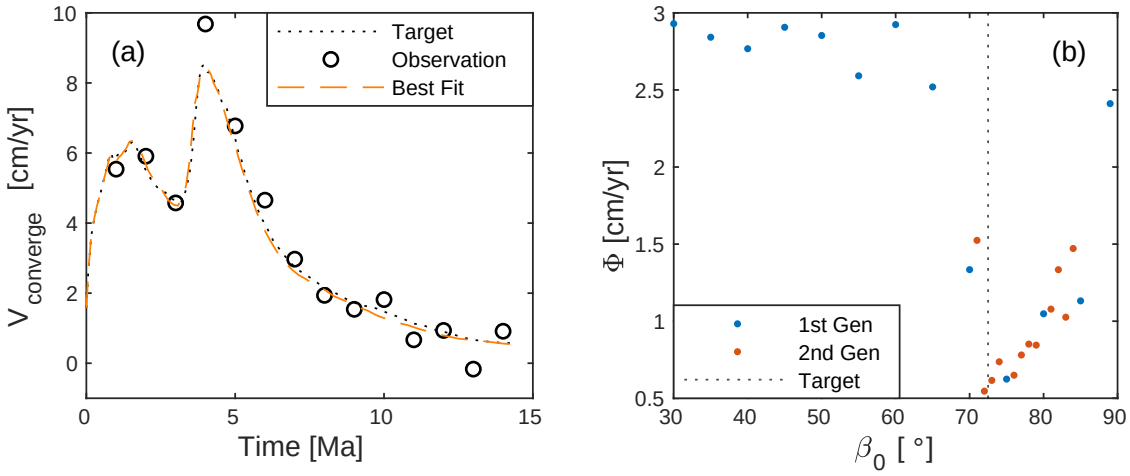

Figure S8. Results of inversion for initial angle (β_0). (a) Dotted black line shows profile of target model ($\beta_0 = 72.5°$) and black circles show noisy observation based on the target model. Dashed orange line shows best fitting model ($\beta_0 = 72°$). (b) RMS misfit (Φ) as a function of β_0. Blue dots shows first set of models in 5° intervals and orange dots show second set in 1° intervals in areas of low misfit. Dotted black line indicates β_0 of the target model.

Table S1. Material parameters for salt application

Material	$\rho\,[\frac{\mathrm{kg}}{\mathrm{m}^3}]$	G [GPa]	$\nu[\,]$	η [Pas]	c_0[MPa]	$\phi[^\circ]$
Crust	2700	30	0.25	10^{24}	10	30
Salt	2200	15	0.25	10^{19}	10	30

Table S2. Material parameters for subduction application

Material	$\rho\,[\frac{\mathrm{kg}}{\mathrm{m}^3}]$	$B_n\,[\frac{1}{\mathrm{MPa}^{-\mathrm{n}}}]$	E_n [kJ]	$V_n\,[\frac{\mathrm{cm}^3}{\mathrm{mol}}]$	$n[\,]$	c_0[MPa]	$\phi[^\circ]$
OP* Crust	2800	6.7 x 10^{-6}	156	0	2.4	10	30
OP* Lithosphere	3250	1.1 x 10^5	530	9.5	3.5	10	30
SP* Lithosphere	3300	1.1 x 10^5	530	9.5	3.5	10	30
Mantle	3300	1.1 x 10^5	530	9.5	3.5	10	30
Weak Zone	3250	$\eta = 10^{20}$ Pas				0.1	5

*OP corresponds to overriding and SP to subducting plate.

Table S3. Scaling parameter ranges

	S_1	S_2	S_3	S_4	Sz
min	0.5	0.5	0.5	0.5	0.8
max	2.0	3.0	2.0	1.5	1.1